Chapter 6

MAPPING HIGH-RESOLUTION LAND SURFACE RADIATIVE FLUXES FROM MODIS: ALGORITHMS AND PRELIMINARY VALIDATION RESULTS

Shunlin Liang, Kaicun Wang, Wenhui Wang, Dongdong Wang, Sheng Gui, Xiaotong Zhang, Jeremy Mirmelstein, Xiufang Zhu, Hye-yun Kim, Juan Du, Steven Running, John Townshend, Si-Chee Tsay, Robert Wolf, Crystal Schaaf, Alan Strahler

6.1 Introduction

Land surface radiative fluxes are needed to address a variety of scientific and application issues related to climate changes, hydrologic and biogeophysical modeling, solar energy applications, and agriculture. The Earth's surface radiation budget (SRB) is the key quantity that determines global climate and climate change from elevated greenhouse gases, air pollution (Wang K. *et al*. 2009), and land cover and land use changes (Wang *et al*. 2007b). The SRB is also important to life and to the use of clean renewable solar energy to improve the quality of the environment.

Altering surface radiation force will lead to a significant adjustment in surface temperature, moisture, and fluxes during the consequent complex land surface thermodynamic and hydrological processes. It affects the surface heat and moisture budget as well as biological productivity. The observed reduction in land surface radiation over the last several decades (1960-1990), the so-called "dimming effect," and the more recent evidence of a reversal in "dimming" over some locations beyond 1990 suggest several consequences on climate, notably on the hydrological cycle (Liepert and Romanou 2005, Wild *et al.* 2005, 2007). Such a reduction in radiation should imply reduced surface temperature and precipitation. Overestimation of the incoming solar radiation over land has major impacts on the climate over land (Betts *et al.* 1996, Dickinson 1995, Garratt *et al.* 1993). Viterbo and Beljaars (1995) found that excessive net radiation at the surface forced excessive surface evaporation, and dried out the soil moisture during data assimilation in the ECMWF (European Centre for Medium-Range Weather Forecasts) global model.

D. Li et al. (eds.), *Geospatial Technology for Earth Observation*,
DOI 10.1007/978-1-4419-0050-0_6,

There are several global radiative flux data sets derived from either satellite observations or GCM (General Circulation Model) reanalysis. The CERES (Clouds and the Earth's Radiant Energy System) Science Team (Wielicki *et al.* 1998) uses cloud and aerosol information from MODIS (Moderate-Resolution Imaging Spectroradiometer) and top-of-atmosphere (TOA) broadband fluxes as a constraint to produce radiative fluxes at the spatial resolution of 140 km. The ISCCP (International Satellite Cloud Climatology Project) has produced a new 18-year (1983-2000) global radiative flux data product called ISCCP FD, every three hours on a 280-km equal-area global grid (Zhang *et al.* 2004). ISCCP FD is calculated using a radiative transfer model from the Goddard Institute for Space Studies (GISS) GCM with the atmosphere and surface properties primarily from the TIROS Operational Vertical Sounding (TOVS) data. The GEWEX SRB Release 2 has a spatial resolution of 1° x 1° and temporal resolution from 3-hour data, daily to monthly from July 1983 to 2007 (Pinker *et al.* 2003,http://www.gewex.org/ssg-21/2009-SSG_GRP-status.pdf). The reanalysis datasets are usually of coarse spatial resolutions (>1°) and fine temporal resolutions, such as those from the NASA DAO (Data Assimilation Office), ECMWF (ERA-40) and NCEP/NCAR (National Centers for Environmental Prediction/ National Center for Atmospheric Research.

Since almost all of these products focus on radiative fluxes at different atmospheric profiles from surface to the TOA, the surface radiative fluxes may not have the accuracy required for land applications. For example, the CERES team uses the predefined albedo and emissivity maps to calculate surface radiative fluxes, which cannot account for their dramatic variations. More importantly, the spatial resolutions of current surface radiative flux products are too coarse to be used for many land applications. For example, the MODIS science team currently has to use the DAO coarse-resolution reanalysis solar radiation product as the forcing data to produce the 1-km PSN/NPP (Photosynthesis/Net Primary Production) product (MOD17) (Zhao *et al*. 2006). The resulting accuracy is not satisfactory and 1-km incident PAR data are a critical need. The hydrological product (Mu *et al.* 2007, Cleugh *et al.* 2007) from MODIS data (MOD16) is also of 1-km resolution, but the meteorological forcing data currently available are quite coarse. As Berg *et al*. (2005) pointed out, bias to many of the reanalysis fields limits their use for hydrological modeling.

One relevant issue is that for coarse spatial resolutions, existence of unresolved sub pixel clouds are crucial. It is actually extremely difficult to quantify the error bounds and uncertainties of the current coarse-resolution SRB products because of the inevitable mismatches with ground “point” measurements in both space and time for validation. The current products have large uncertainties. On a daily basis, the estimate of the solar incoming shortwave radiation from GOES (Geostationary Operational Environmental Satellite) data has an uncertainty of approximately 10%, but at shorter time increments, for example hourly, the uncertainty is much greater (on the order of 20-30%), especially for partly cloudy conditions. The SRB errors for shortwave and longwave over snow and ice surfaces and for longwave in persistently cloudy regions are larger than those in other regions (Pinker *et al.*

2003). Raschke *et al*. (2006) examined ISCCP and GEWEX (Global Energy and Water Cycle Experiment)-SRB data sets and found that there are serious errors in ancillary data that lead to large uncertainty in the final products and they recommended complete reprocessing. Hicke *et al*. (2005) found that mean global NCEP solar radiation exceeded that from GISS by 16%, likely due to lower cloudiness within the NCEP reanalysis compared to satellite observations. Locally, relative differences were up to 40% in the mean and 10% in the trend of solar radiation and NPP, and varied in sign across the globe.

Because of the improved spatial and spectral resolutions of the MODIS solar and IR imager and an available suite of high-level land and atmosphere standard products, we anticipate a significant improvement of radiative flux estimates from the kilometer-scale MODIS observations. They will be extremely useful in driving high-resolution land ecosystem/carbon cycle and hydrological models, and validating the coarse resolution SRB products for improved water and energy fluxes. However, the EOS (Earth Observing System) standard products from MODIS include only certain components of SRB (e.g., broadband albedo, spectral emissivity and skin temperature).

In this chapter, we describe the algorithms for generating all land surface radiative fluxes from MODIS data, including incident insolation and PAR (Photosynthetically-Active Radiation), shortwave net radiation, clear-sky longwave downward and upward radiation, and all-wave all-sky net radiation. The validation results are also presented. The overview of these algorithms is shown in Figure 1, and the individual algorithms are discussed below in details. Measurements collected at about 100 sites globally are being used to validate the algorithms described here. These measurements are collected from different networks, including SURFRAD (Surface Radiation Budget Network), ARM (Atmospheric Radiation Measurement), FLUXNET (Ameriflux, Euroflux and Asiaflux), GAME ANN (GEWEX Asian Monsoon Experiment, in which GEWEX stands for Global Energy and Water cycle Experiment, Asian Automatic Weather Station Network) and AERONET (AErosol RObotic NETwork). The land cover types of these sites include desert, cropland, grassland, and forest. The locations of the sites vary from tropical to temperate and polar areas, with elevations ranging from near sea level to about 5 km high on the Tibetan Plateau.

6.2 All-Sky Incident PAR and Insolation

6.2.1 Background

Incident solar radiation, either PAR in the visible spectrum (400-700 nm) or insolation in the total shortwave (300-4000 nm), is a key variable required by almost all land surface models. Many ecosystem models calculate biomass accumulation linearly proportional to incident PAR. Information on the spatial and temporal distribution of PAR, by control of the photosynthesis and transpiration process, is re-

quired for modeling the hydrological cycle and for estimating global oceanic and terrestrial net NPP.

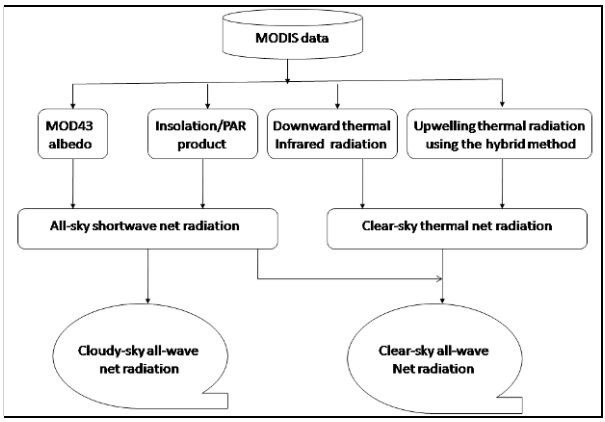

Fig. 6.1 Flowchart of the estimation of net radiation flux from MODIS

The only practical means of obtaining incident PAR/insolation at spatial and temporal resolutions appropriate for most modeling applications is through remote sensing. The existing products normally have high temporal resolutions (around 3 hours) but coarse spatial resolutions (around 1°). They are primarily suitable for climate modeling and analysis.

Because the high-resolution incident PAR/insolation over land surfaces is not a standard EOS product, the MODIS science team has to disaggregate the NASA data assimilation PAR product of three-hourly 1º by 1.5º spatial resolution to produce 1-km NPP and net PSN products using the BIOME-BGC model (Running *et al.* 1999, Running *et al.* 2004). The simplified PAR flux models have been used to produce the incident PAR flux over oceans using MODIS data (Carder *et al.* 1999) and SeaWiFS (Sea-viewing Wide Field-of-view Sensor) data (Frouin *et al.* 2000). No PAR product has been routinely generated from MODIS data over land by NASA. The incident PAR product constitutes a major uncertainty in carbon cycle modeling.

Satellite TOA observations contain information from both the atmosphere and the land surface. The current methods (Carder *et al.* 1999, Frouin *et al.* 2000, Gu *et al.* 2004, Pinker and Laszlo 1992, Pinker *et al.* 2003) assume that either the atmospheric information is available from other sources (e.g., the ISCCP PAR product with atmospheric climatology data as input) or water surface reflectances are known (e.g., SeaWiFS and MODIS PAR products over oceans).

If the atmospheric parameters and surface spectral albedos are known, the existing algorithms for MODIS (e.g., van Laake and Sanchez-Azofeifa 2004, 2005) may be directly applied. However, these models are based on rudimentary two-stream approximations for multiple scattering or even simpler schemes. Computation is speeded up significantly with the simplified models, but they usually are

not accurate in calculating multiple scattering that dominates when the atmospheric optical depth is large (hazy or cloudy) and/or the surface is very bright (snow/ice). Simple models are easy to implement, and suitable for cases where no accurate input parameters are available (e.g., processing GOES data alone). Increasing the model complexity increases difficulties of implementation for regional and global applications. Furthermore, the MODIS aerosol optical depth products have much coarser spatial resolution (~10km) and contain many gaps over land surfaces (Remer *et al*. 2005, 2008). Therefore, the method of van Laake and Sanchez-Azofeifa is not suitable for estimating incident PAR from MODIS data at 1-km resolution.

Another issue is the separation of direct and diffuse PAR radiation. The volume of shade within vegetation canopies is reduced by more than an order of magnitude on cloudy and/or very hazy days compared to clear, sunny days because of an increase in the diffuse fraction of the solar radiance. In a recent study, Gu *et al*. (2002) found that: (1) diffuse radiation results in higher light use efficiencies by plant canopies; (2) diffuse radiation has much less tendency to cause canopy photosynthetic saturation; (3) the advantages of diffuse radiation over direct radiation increase with radiation level; and (4) temperature as well as vapor pressure deficit can cause different responses in diffuse and direct canopy photosynthesis, indicating that their impacts on terrestrial ecosystem carbon assimilation may depend on radiation regimes and thus sky conditions. Wang K. *et al*. (2008b) provided observational evidence that diffuse radiation results in not only higher light use efficiencies but also higher evaporative fractions. These findings call for different treatments of diffuse and direct radiation in models of global primary production, and studies of the roles of clouds and aerosols in the global carbon cycle (Gu *et al*. 2003). In fact, many land surface process models, such as SiB2 (Simple Biosphere Model, Sellers *et al*. 1996) and CLM (Community Land Model, Dai *et al*. 2003), separate direct and diffuse solar radiation. However, none of the existing PAR products separate these two components.

A new algorithm for estimating incident PAR and insolation from MODIS data using the look-up table (LUT) approach has been developed (Liang *et al*. 2006). It has been revised to map incident PAR over China (Liu *et al*. 2008). This algorithm has also been extended to GOES data (Zheng *et al*. 2008, Wang D. *et al*. 2009b) and is being altered for other satellite data (Liang *et al*. 2007). Although this algorithm was primarily designed for mapping incident PAR, insolation is one of the outputs. We have further refined the algorithms specifically for PAR and insolation, and the details are given below.

6.2.2 All-sky PAR

6.2.2.1 Instantaneous PAR

Incident PAR depends mainly on atmospheric properties, but also to a lesser extent on surface reflectance. It can be demonstrated by the following formula for

calculating downward spectral flux $F(\mu_0)$ at the solar zenith angle θ_0 ($\mu_0 = \cos(\theta_0)$) over a Lambertian surface (Chandrasekhar 1960, Liang, 2004):

$$F(\mu_0) = F_0(\mu_0) + \frac{r_s \overline{\rho}}{1 - r_s \overline{\rho}} \cdot E_0 \cdot \mu_0 \cdot \gamma(\mu_0) \tag{6.1}$$

where $F_0(\mu_0)$ is the downward flux without any contributions from the surface, r_s is surface reflectance, $F(\mu_0)$ spherical albedo of the atmosphere, E_0 is the extraterrestrial solar irradiance, $\gamma(\mu_0)$ is the total transmittance (direct plus diffuse) in the solar illumination direction. It is clear that the surface contribution to the incident PAR mainly depends on $r_s \overline{\rho}$. If the atmosphere is very clear (i.e., $\overline{\rho}$ is small) or the surface reflectance r_s is low, the surface contribution to the incident PAR is relatively small.

All radiometric variables are functions of wavelength. PAR is the integration of the downward spectral fluxes from 400 nm to 700 nm:

$$PAR(\mu_0) = \int_{400}^{700} F_\lambda(\mu_0) d\lambda \tag{6.2}$$

We use the energy unit Wm^{-2} in our LUT. Note that many ecosystem process models typically employ PAR data in quantum units (photosynthetic photon flux density, μ mol m^{-2} s^{-2}) and the conversion between the energy units to the quantum units was discussed by Dye (2004).

Our method first estimates surface reflectance from multi-temporal imagery and then appraises PAR flux for each imagery. The basic procedure is composed of two steps, including (1) determination of the surface reflectance from observations under 'clearest atmospheric conditions during a temporal window and (2) calculation of incident PAR from the determined surface reflectance and TOA radiance/reflectance using the LUT approach. Determining the length of the temporal window needs to be done carefully. Obviously, it must be short enough so the surface properties do not change dramatically, but long enough to include adequate observations under clear conditions. In all our case studies, it seems a period of one to three months is a reasonable choice.

Most PAR algorithms do not consider surface topography. Evaluating the significance of this omission, Winslow *et al*. (2001) found that the ISCCP-PL PAR product in mountainous regions was underestimated in comparison to long-term radiation climatologies. This is particularly relevant for carbon cycle modeling when the spatial resolution increases since many forests are distributed over mountainous regions. We could add a new dimension to the LUT, but it would make the process much more complicated. We have incorporated topographic correction in our PAR mapping from GOES (Zheng *et al*. 2008), and the new elevation adjustment to the instantaneous PAR from MODIS is presented here.

In the PAR spectral region, surface elevation influences the atmospheric mass that in turn affects Rayleigh scattering transmittance. In creating the LUT to esti-

mate PAR, surface elevation was set at sea level. Ignoring the influence of elevation may introduce substantial errors in PAR retrieval. Since the impacts of aerosol and clouds are considered in the original algorithm, the elevation effect on Rayleigh scattering is considered. To quantify this influence, the normalized transmittance is defined as follow:

$$T_n = \frac{T_{ray,z}}{T_{ray,0}} \tag{6.3}$$

where $T_{ray,z}$ is the Rayleigh scattering transmittance at an elevation of z in km and $T_{ray,0}$ is the Rayleigh scattering transmittance at sea level. We calculate the normalized transmittance using an atmospheric radiative transfer model, 6S (Vermote *et al*. 1997).

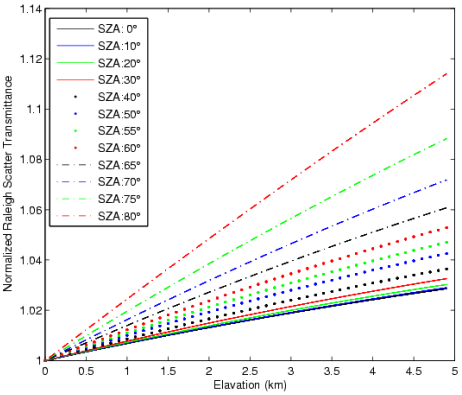

Fig. 6.2 Normalized Rayleigh scattering transmittance (Equation (3)) as a function of surface elevation and solar zenith angle

Figure 6.2 shows that the normalized transmittance is the function of surface elevation and the solar zenith angle. It is shown that PAR can be under-estimated up to 10% for highlands. This effect has not been addressed in the current algorithms to estimate surface solar radiation and PAR. Study has shown that the systematic underestimation of solar radiation products over the Tibetan Plateau (elevation is higher than 4000 m for the most part) perhaps resulted from ignoring the elevation effect (Yang *et al*., 2006). Figure 6.2 illustrates that it is essential to incorporate the effect of surface elevation. However, since including surface elevation into an LUT explicitly as one dimension will substantially increase the computational time in searching for the LUT, we apply an empirical regression to correct for the influence of elevation on Rayleigh scattering:

$$T_n = 1 + \frac{1}{18.56 + 121.55 \cdot \cos(\mu_s)} \cdot z - 0.00035 \cdot z^2 \tag{6.4}$$

where μ_s is the cosine of the solar zenith angle (less than 85º), and z is surface elevation in km. Equation (6.4) predicts the normalized transmittance with a correla-

tion coefficient of 0.9998, a bias of 0.000085 and a standard deviation of 0.00037. Surface elevation data used here are from GTOPO30 at a spatial resolution of 30 arc seconds (http://edc.usgs.gov/products/elevation/gtopo30/gtopo30.html).

Although PAR flux is less dependant on surface reflectance, we need to consider an abrupt significant change of surface reflectance. The extreme case is snowfall and snowmelt. The snow observations have to be labeled and separated from non-snow observations. They must be processed separately but in the same fashion. The MODIS team is routinely producing snow and ice cover maps. These maps can be used to distinguish snow and cloud, which has been an issue in previous studies (e.g., Pinker *et al*., 2003). Our algorithm separates snow and non-snow observations using the MODIS snow cover maps and applies the same procedures to these two groups of observations separately.

The validation results had been published (Liang *et al*. 2006, 2007). The validation exercises were conducted using ground measurements of incident PAR at six FLUXNET sites (Fort Peck, Montana; Lost Creek, Wisconsin; Oak Ridge, Tennessee; Walker Branch, Tennessee; Santa Rem, Brazil; and Black Hills, South Dakota) from 2002-2004. For each site, a 3km x 3km window (9 pixels) of the MODIS TOA radiance (MOD02) and angular values were extracted from the MODIS datasets ordered from the EOS Gateway. The ground measurements collected every half-hour or one hour were compared with the retrieved values. The measurement values closest to the time of MODIS data acquisition were used to compare with the value of the central pixel in the extracted 9-pixel window without any interpolation.

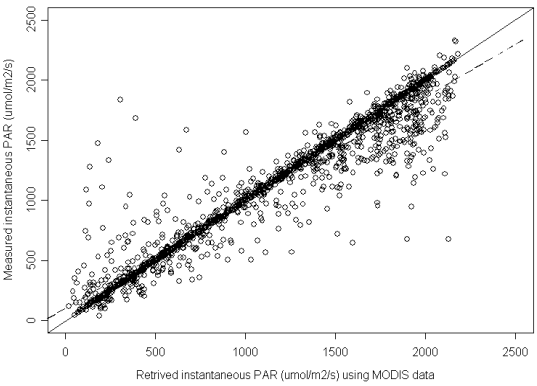

Fig. 6.3 Validation of MODIS-derived instantaneous PAR data at six FLUXNET sites. The solid line is the 1:1 line, the dashed line is the best fit line based on least squares regression.

6.2.2.2 Daily PAR

Daily-integrated PAR is more useful than instantaneous PAR in many cases because many ecosystem models require a daily or coarser temporal resolution. MODIS acquires data from both Terra and Aqua satellites, and the number of overpasses depends on geographical location. Multiple observations are used for

calculating daily PAR. A regression method was proposed in our original algorithm (Liang *et al*., 2006), but we found later that the LUT method performs much better (Wang, D. *et al*., 2009).

When estimating instantaneous PAR, atmospheric visibility is stored in the LUT as an intermediate quantity. The visibility values at any other times are interpolated based on these recorded visibility values for the instantaneous PAR. If there is only one observation on a given day, the visibility value estimated at the overpass time is used for the entire day. If there are more than one observation per day, the first visibility value is used for the time before the first overpass time and the last visibility value is used for the time after the last overpass time; the visibility value at other times is linearly interpolated:

$$\begin{aligned} VV_t &= VV_{T_n} \cdot (1-p) + VV_{T_{n+1}} \cdot p \\ p &= \frac{t - T_n}{T_{n+1} - T_n} \end{aligned} \tag{6.5}$$

where VV_t is the interpolated visibility value at time t, T_n and T_{n+1} are the two satellite overpass times immediately before and after t, and VV_{T_n} and $VV_{T_{n+1}}$ are the corresponding visibility values estimated from satellite observations.

After obtaining the visibility value at a given time, we can estimate PAR at the moment. To maximize computation efficiency, we calculate the instantaneous PAR values at 30-minute intervals. Daily PAR is obtained by integrating the 30-minute instantaneous PAR values:

$$\begin{aligned} DailyPAR &= \sum_{t=1}^{N} InstPAR(t)\Delta t \\ N &= (T_{sunset} - T_{sunrise})/\Delta t + 1 \end{aligned} \tag{6.6}$$

where N is the number of instantaneous PAR values used to calculate daily PAR, Δt is the time interval, $InstPAR(t)$ is the instantaneous PAR at time t, calculated with the interpolated visibility value.

The validation results have been presented elsewhere in details (Wang D. *et al*. 2009). Figure 6.4 shows a comparison of field-measured and MODIS-estimated daily-integrated total PAR at ten AmeriFlux stations using the LUT method (Table 6.1), which is better than the sinusoidal method. It demonstrates that MODIS data alone adequately capture the diurnal variations of incident PAR at high latitudes where the number of MODIS overpasses is large. Generally, the estimated values correlate well with field-measured values, and the average R^2 value is 0.927. The average RMSE is 1121.8 kJ/m^2/day.

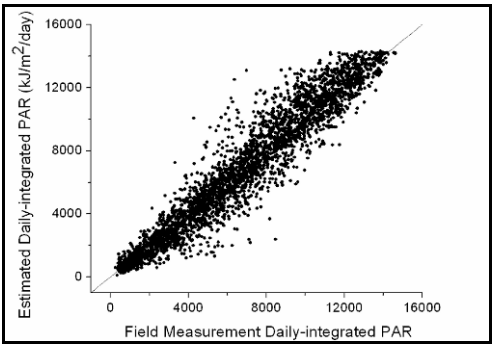

Fig. 6.4 Scatterplots of field-measured and MODIS daily-integrated PAR at 10 AmeriFlux stations

Table 6.1 Comparison of validation results for the adjusted sinusoidal interpolation (SIN) and look-up table (LUT) methods at the ten AmeriFlux stations

Station	R square		RMSE		Bias		Relative Error	
No	SIN	LUT	SIN	LUT	SIN	LUT	SIN	LUT
1	0.887	0.891	1392.8	1090.0	645.8	21.5	14.7%	12.6%
2	0.863	0.873	2125.5	1544.2	1535.3	911.3	26.4%	19.1%
3	0.933	0.937	1138.2	955.8	420.3	-227.6	11.9%	10.8%
4	0.936	0.941	1643.7	1079.9	1125.4	508.9	19.8%	14.2%
5	0.953	0.950	1266.1	863.2	668.6	-45.1	12.2%	10.2%
6	0.952	0.949	1854.5	1234.4	1363.8	719.8	25.3%	18.2%
7	0.927	0.925	1313.6	1252.3	83.2	-560.9	19.8%	19.5%
8	0.942	0.940	1305.0	985.4	541.3	-74.1	19.2%	15.9%
9	0.947	0.943	1137.4	1030.7	279.4	-383.2	15.7%	15.8%
10	0.927	0.925	1319.3	1181.9	291.4	-502.3	19.3%	19.2%
Average	0.927	0.927	1449.6	1121.8	695.4	36.8	18.4%	15.6%

The temporal-scaling approach of the LUT is able to scale both diffuse and direct portions accurately as well. Diffuse PAR is not a standard measurement at AmeriFlux stations, so we cannot perform an extensive validation for diffuse radiation. We chose the Bartlett Experimental Forest, New Hampshire station (44°3'52.7" N, 71°17'17.1" W) to evaluate the performance of our LUT method. An experimental forest of the US Forest Service, the Bartlett Forest is a northern temperate hardwood forest consisting primarily of American beech, red maple, paper birch and hemlock trees. We used the diffuse and total PAR measured in 2005 at Bartlett Forest to validate our algorithm (Figure 6.5). The validation result for total PAR is similar to PAR at the other stations. Diffuse radiation was not as accurately estimated at Bartlett Forest compared to total radiation based on R^2 and bias.

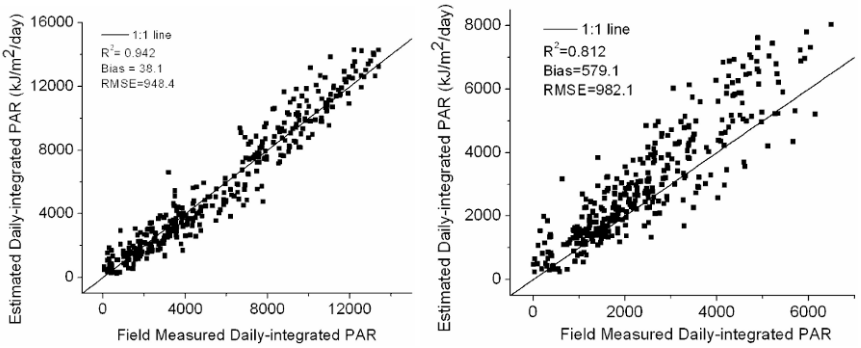

Fig. 6.5 Comparison of field-measured and MODIS-estimated daily-integrated PAR at Bartlett Experimental Forest: total PAR (left), and diffuse PAR (right).

The LUT method has been employed to produce a three-year (2003-2005) daily-integrated PAR product over North America that is being distributed through ORNL DAAC (Oak Ridge National Laboratory Distributed Active Archive Center). Figure 6.6 is the map of daily-integrated PAR compared with GOES PAR for June 3-6, 2003. PAR values are generally high because the solar zenith angle is small and the number of daylight hours is large. Clouds have a strong effect on PAR values. Cloud patterns from MODIS daily-integrated PAR correlate well with GOES patterns. The GOES PAR map is relatively smooth because GOES observes the surface with greater frequency, thus fragmented clouds are usually averaged over time. We calculated the relative difference, D , to better illustrate the difference between MODIS PAR and GOES PAR:

$$D=\frac{2(PAR_{MODIS}-PAR_{GOES})}{(PAR_{MODIS}+PAR_{GOES})} \qquad (6.7)$$

Figure 6.6 shows that there is little relative difference between MODIS and GOES for most areas. Although daily-integrated GOES and MODIS PAR correlate well, there are differences between the two datasets. The greatest difference occurs near cloud boundaries because cloud patterns are highly variable near cloud boundaries. A small number of MODIS observations per day cannot accurately record variable daily cloud conditions. If the sky is overcast at the time of a single MODIS overpass, the algorithm classifies the entire day as overcast and daily-integrated PAR is underestimated. Overestimation of daily-integrated PAR occurs when the sky is clear at the time of the MODIS overpass, but cloudy at other times during that day. Figure 6.7 gives an example of the monthly incident PAR over North America in 2003.

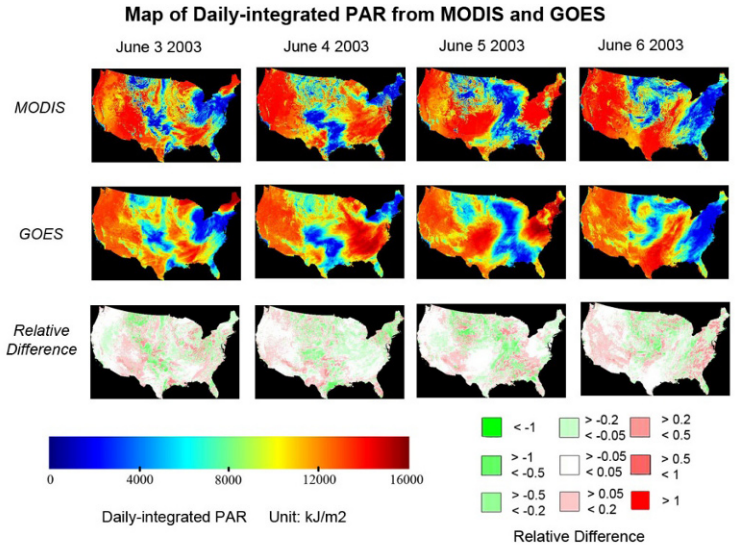

Fig. 6.6 Comparison of MODIS and GOES daily-integrated PAR and relative difference maps of the conterminous United States for June 3-6, 2003.

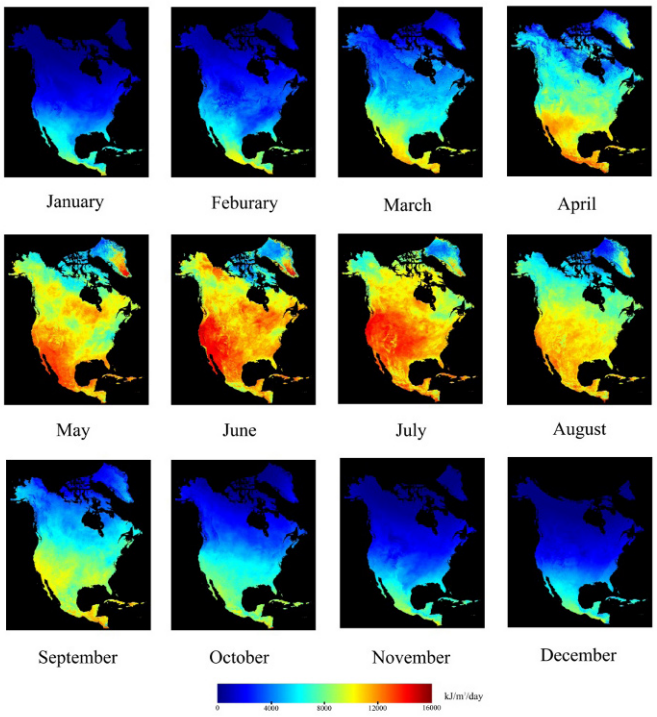

Fig. 6.7 Monthly incident PAR over North America continent in 2003

6.2.3 All-sky Insolation

Insolation is outputted from the LUT in the same way as incident PAR. Here we further consider atmospheric water vapor effects. We could add atmospheric water vapor as another dimension in the LUT, but a simpler parameterization is desirable. The atmospheric water vapor transmittance for insolation has been examined for quite some times, and many parameterizations can be found in the literature, for example,

(1) water vapor transmittance is calculated as (Duchon and Malley 1999):

$$T_W = 1 - 0.077 \cdot (u \cdot m)^{0.3} \tag{6.8}$$

where u is water vapor amount in cm, m is atmospheric mass at surface:

$$m = \frac{35}{\sqrt{1224 \cdot \cos(\theta_S)^2 + 1}} \tag{6.9}$$

where θ_S is solar zenith angle.

(2) water vapor transmittance is calculated as (Annear and Wells 2007):

$$T_W = 1 - \frac{2.4959 \cdot (u \cdot m)}{(1 + 79.034 \cdot (u \cdot m))^{0.6828} + 0.6385 \cdot (u \cdot m)} \tag{6.10}$$

We evaluated the above parameterizations with the atmospheric radiation model 6S (Vermote *et al*. 1997) simulation. Figure 6.8 shows a comparison between the 6S simulated water vapor transmittance and simplified Equation (6.8). It appears equation (6.8) has a systematic overestimation compared with the 6S simulation. Figure 6.9 shows a comparison between the 6S simulated water vapor transmittance and simplified equation (6.10) that appears to have a systematical underestimation.

Because of their significant differences with the 6S simulation results, we have derived a new formula that works much better than the previously mentioned methods:

$$T_W = \sqrt{0.8197 - 0.07066 \cdot \lg(u \cdot m)} \tag{6.11}$$

Figure 6.10 shows a comparison between the 6S simulated water vapor transmittance and simplified equation (6.11). There is no bias, and the RMSE is 0.0036.

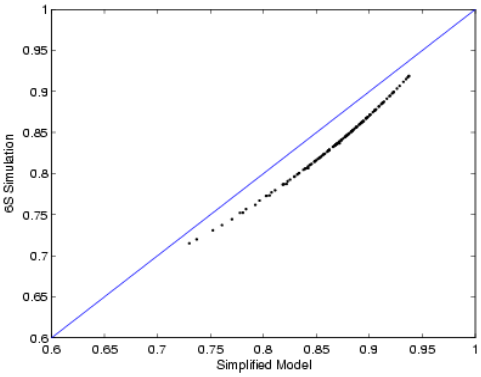

Fig. 6.8 Comparison between the 6S simulated water vapor transmittance and equation (6.7). The bias is 0.0304, and the RMSE is 0.0041.

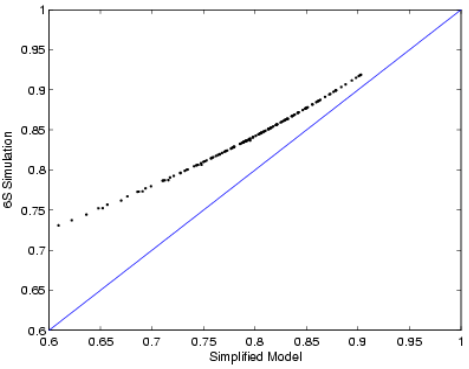

Fig. 6.9 Comparison between the 6S simulated water vapor transmittance and equation (6.9). The bias is -0.0481, and the RMSE is 0.0239.

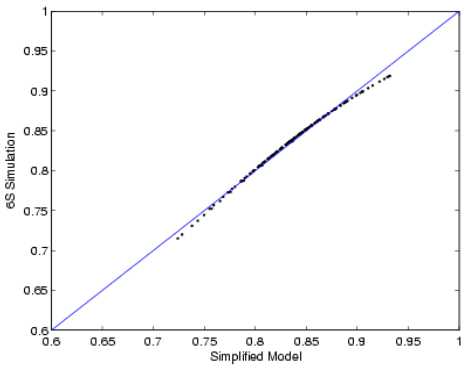

Fig. 6.10 Comparison between the 6S simulated water vapor transmittance and simplified equation (6.11).

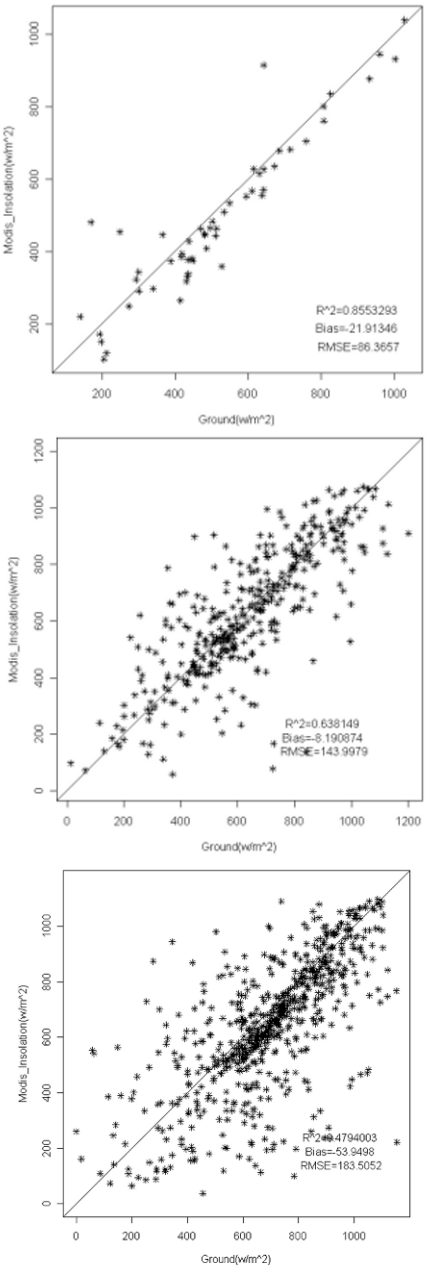

Fig. 6.11 Comparison of MODIS insolation retrieval (y-axis) and ground measurements (x-axis) in 2000 at Dunhuang (top), D66 (middle) and Amdo in 2000-2003 (bottom).

Yang *et al*. (2008) evaluated some state-of-the-art satellite products of incident insolation over the Tibetan Plateau. Their results show that the current satellite products have substantial uncertainty over the Tibetan Plateau area. Here we present our preliminary validation results over the Tibetan Plateau. Ground measurements at three sites were selected: (1) Amdo (32.241N, 91.625E) has a surface elevation of 4700 m and a land surface type of grassland, (2) Dunhuang (40.15N, 94.683E) has a surface elevation of 1140 m and is located in a desert oasis (grassland and cropland), and (3) D66 (35.523N, 93.785E) has a surface elevation of 4600 m and is located in desert. The 30-minute-average insolation data were downloaded from (http://aan.suiri.tsukuba.ac.jp/aan-center.html). We compared the 30-minute measurements with our MODIS retrievals, and the results are shown in Figure 6.11. Table 6.2 summarizes the evaluation results of our MODIS insolation products and other satellite insolation products reported by Yang *et al*. (2008). The GEWEX insolation product clearly exhibits substantial biases, because this product does not account for the elevation effect on the insolation as discussed in Section 6.2.3. Table 6.2 shows that the MODIS insolation product has a much smaller RMSE compared to other satellite insolation products over the Tibetan Plateau.

Table 6.2 Summary of the validation results of current satellite products of hourly incident insolation over the Tibetan Plateau. *: calculated from Table 3 in Yang *et al*. (2008)

Products	Spatial resolution	Temporal resolution	Relative bias	Relative RMSE
GEWEX V2.5*	1º	3 hour	-19.9%	41.4%
GEWEX V2.81*	1º	3 hour	6.5%	33.7%
ISCCP-FD*	2.5º	3 hour	-4.7%	35.4%
University of Maryland -SRB*	0.125º	1 hour	-0.4%	36%
MODIS	1 km	Instantaneous	-4.4%	21.9%

6.2.4 All-sky shortwave net radiation

Surface shortwave net radiation can be calculated from insolation (F_d^s) and upward radiation or the total shortwave broadband albedo (α):

$$S_n = F_d^s - F_u^s = F_d^s(1-\alpha)$$

Assuming we can accurately map insolation, calculation of shortwave net radiation now becomes albedo mapping. Global surface broadband albedo is a standard MODIS product and has been generated routinely from MODIS data every 8 days (MOD43) (Schaaf *et al*., 2002). We can combine it with the insolation estimate to obtain incident shortwave net radiation.

6.3 Clear-sky Downward Longwave Radiation

Downward longwave radition (F_d^l) is a critical component in energy balance calculations. There have been several comprehensive reviews of methods for estimating the surface thermal radiation (Diak *et al.* 2004, Ellingson 1995, Schmetz 1989). The downward longwave radiation algorithms include three types (Darnell *et al*. 1986, Gupta *et al*. 1992). *The first* is empirical functions using satellite-derived meteorological parameters, for example, the near-surface temperatures and water vapor burden. *The second* is to calculate the radiation quantities with radiative transfer models using satellite-derived soundings. A strong feature of this approach is the validity of the physics. *The third* is to use satellite observed radiances directly to avoid the propagation of retrieval errors of meteorological parameters into the final radiation estimate (Lee and Ellingson 2002). It embeds the physical merits of the radiative transfer within the parameterization of nonlinear functions of observed radiance.

It is straightforward to calculate F_d^l using atmosphere profiles and a radiative transfer model. However, the physical method is sensitive to the errors in the atmosphere profile. F_d^l is dominated by the radiation from a shallow layer that is close to the earth surface. The contribution from the atmosphere above 500 m from the surface only accounts for 16-20% of total F_d^l (Schmetz 1989). The vertical resolution of the MODIS-retrieved atmosphere profiles is too coarse. Only 5 layers are available between 1000 - 800 hPa pressure levels and the detailed structures of the atmosphere cannot be captured (Seemann *et al*. 2003). Our recent study (Wang W. and Liang 2009) showed that F_d^l cannot be estimated with acceptable accuracy using the MODIS atmospheric profile product, especially over high elevation surfaces. For example, we compared F_d^l calculated from the MODIS atmospheric profile product and ground-based measurements at two SURFRAD sites: Sioux Falls (473 m) and Boulder (1689 m). The errors at both sites are larger than 20 W/m^2, and the RMSE at the Boulder site is 37.26 W/m^2.

Consequently, we developed a new hybrid algorithm that combines extensive radiative transfer simulation (physical) and regression analysis (statistical). Validation results indicate that it performs very well (Wang W. and Liang, 2009).

6.3.1 Radiative Transfer Simulation

The MODIS Terra atmosphere product was used to establish the atmosphere profiles database needed in radiative transfer simulation of TIR (Thermal Infrared) TOA radiances and F_d^l to derive statistical relationships. The database consists of more than 8000 representative profiles. Ts, surface pressure, column water vapor, elevation, and Ta (derived from the temperature profile) corresponding to each profile were also included in the database to facilitate method development.

The plant function type for each atmosphere profile was determined using the co-located MODIS land cover product. The Johns Hopkins University (JHU)

emissivity spectra in the ASTER (Advanced Spaceborne Thermal Emission and Reflection Radiometer) Spectral Library (ASTER, 1999) were used to approximate spectral emissivity for each plant function type.

MODTRAN4 (MODerate spectral resolution atmospheric TRANSsmittance, Berk *et al*. 1999) was used in the radiative transfer simulation. F_d^l, spectral F_d^l, thermal path radiance, and surface-TOA transmittance were simulated for each atmosphere profile. Thermal path radiance and transmittance were calculated at 0°, 15°, 30°, 45°, and 60° sensor view zenith angles. Surface temperature was assigned using T_s from the MODIS atmosphere product. A Lambertian surface was assumed in the simulation. Spectral surface emissions were calculated using Planck's function and emissivity spectra. MODIS TOA radiances were synthesized using spectral F_d^l, spectral surface emission, emissivity spectra, thermal path radiance, surface-TOA transmittance, and MODIS Terra spectral response function.

6.3.2 Regression Analysis

Previous studies indicate F_d^l can be modeled using a linear combination of thermal-IR TOA radiances (Smith and Wolfe 1983, Morcrette and Deschamps 1986). MODIS channels 27-29 and 31-34 are most valuable for predicting F_d^l. This is consistent with the physics that govern F_d^l: 27 and 29 are water vapor channels; 33 and 34 are air temperature profile channels; 29, 31, and 32 are used for retrieving land surface skin temperature (T_s). Near-surface air temperature (T_a) is one of the dominant factors for clear-sky F_d^l. Ts channels are important for estimating F_d^l because it is closely correlated to T_a. However, the daytime and nighttime relationships between T_a and T_s differ, especially over bare ground and high elevation surfaces. Therefore, separate models were developed to predict F_d^l for daytime and nighttime.

Surface pressure is also an important factor in estimating F_d^l because of the effect of the pressure broadening of the spectral lines (Lee and Ellingson 2002). Surface pressure has not been included in the F_d^l models in previous studies. We used elevation (H) as a surrogate for surface pressure to account for the surface pressure effect. The nonlinear F_d^l model was developed to account for the nonlinear effect (Wang W. and Liang, 2009):

$$F_d^l = L_{Tair}\left(a_0 + a_1 L_{27} + a_2 L_{29} + a_3 L_{33} + a_4 L_{34} + b_1 \frac{L_{32}}{L_{31}} + b_2 \frac{L_{33}}{L_{32}} + b_3 \frac{L_{28}}{L_{31}} + c_1 H\right) \tag{6.12}$$

where L_{Tair} equals L_{31} in the nighttime models and equals L_{32} in the daytime models; a_i, b_i, and c_1 are regression coefficients. The nighttime nonlinear model explains more than 93 % of the variation, with standard errors less than 14.90

(nighttime) and 15.20 (daytime) W/m^2. Table 6.3 shows nonlinear model fitting results and the regression coefficients of the nonlinear models are given in Table 6.4.

Table 6.3 Nonlinear downward longwave radiation model fitting results (Standard error unit W/m^2).

	Linear			
θ	Daytime		Nighttime	
	R^2	Std. Err.	R^2	Std. Err.
0º	0.939	14.44	0.943	13.98
15º	0.938	14.47	0.942	14.01
30º	0.938	14.55	0.943	14.10
45º	0.936	14.74	0.940	14.32
60 º	0.932	15.20	0.936	14.79

Table 6.4 Nonlinear downward longwvae radiation model regression coefficients.

	Daytime					Nighttime				
	0º	15º	30º	45º	60 º	0º	15º	30º	45º	60 º
a0	150.20	153.15	162.14	180.91	214.23	84.14	87.07	95.44	112.65	142.44
a1	4.45	4.34	3.91	3.12	2.13	5.37	5.27	4.90	4.18	3.05
a2	-1.74	-1.80	-1.99	-2.41	-3.28	-1.78	-1.83	-1.99	-2.37	-3.20
a3	-21.03	-20.37	-18.46	-14.02	-3.72	-15.51	-14.87	-13.07	-8.88	0.43
a4	32.22	31.68	30.23	-26.55	16.93	27.08	26.52	25.07	21.51	13.06
b1	-150.87	-154.97	-167.04	-192.69	-239.24	-106.53	-110.08	-119.87	-140.71	-177.34
b2	33.18	34.01	35.64	40.59	53.68	62.67	63.05	63.20	64.90	69.79
b3	-26.81	-25.89	-22.38	-16.07	-6.78	-40.55	-39.73	36.61	-30.99	-21.95
c1	-1.91	-1.91	-1.90	-1.91	-1.99	-1.98	-1.98	-1.97	-1.96	-2.00

6.3.3 Validation Results

The nonlinear F_d^l model was first evaluated using MODIS Terra TOA radiances and co-located SURFRAD ground data. To make the MODIS-derived and ground-measured F_d^l comparable, the model was adapted to predict F_d^l in the spectral range of 4 - 50 μm. The error caused by the spectral range difference between the F_d^l model and ground instruments is less than 0.5%, smaller than ground instrument uncertainty. F_d^l for different view zenith angles was derived using linear interpolation. Clear-sky observations were identified using the MODIS cloud product. We also examined all data points manually to exclude cloud-contaminated pixels with unreasonably low TOA radiance values in MODIS channel 31.

The statistics of validation results using Terra data are summarized in Table 6.5. Figure 6.12 shows the validation plots. RMSEs vary from 14.35 to 20.35 W/m^2 and biases from -6.88 to 9.72 W/m^2. Analysis of the preliminary spatial scaling shows that RMSEs were further reduced by 2 W/m^2 after the nonlinear model-predicted F_d^l was aggregated to 5 km and beyond. Our predicted F_d^l is more

accurate than the existing F_d^l products (21-33 W/m^2, monthly) (Wielicki *et al*. 1996, ASDC 2006, Francis and Secora 2004).

Table 6.5 Summary of validation results using MODIS terra and aqua data (unit: W/m2)

Sites	Terra		Aqua	
	Bias	RMSE	Bias	RMSE
Bondville	-9.49	17.75	-7.36	14.98
Sioux Falls	-13.55	17.87	-12.81	17.74
PennState	-7.32	12.72	-5.21	10.92
DesertRock	-21.93	25.03	-20.21	23.94
FortPeck	-8.88	17.46	-7.33	15.11
Boulder	-4.62	19.24	-5.50	18.76
Mean	-10.97	18.35	-9.74	16.91

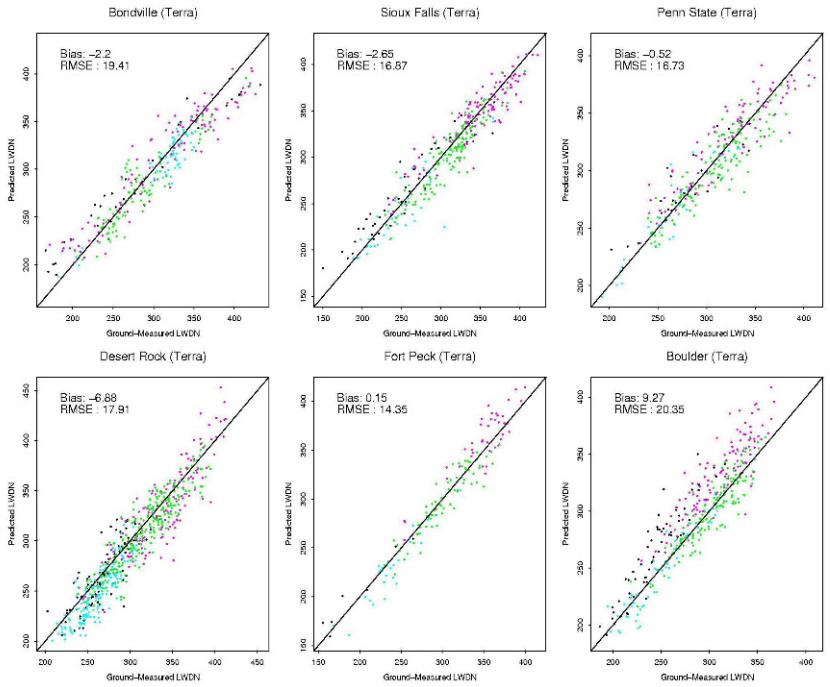

Fig. 6.12 Nonlinear LWDN (downwelling longwave radiation) models validation results using MODIS Terra data (black-fallwinter/day; cyan-fallwinter/night; magenta – springsummer/day; green- spring summer/night).

The spatial mismatch between the MODIS footprint (1 km at nadir) and the ground PIR footprint (~ 200 m) may be a potential cause of the larger scattering during daytime in the model validation results. The Earth's land surface behaves almost as an isothermal and homogeneous surface during nighttime. During daytime, T_S can exceed T_a by more than 20°K (Wan and Dozier 1996). Although MODIS channel 32, rather than channel 31, was used in the daytime nonlinear models, it is still sensitive to T_S.

Cloud contamination may be a significant source of error in this study. The MODIS cloud product cannot mask clouds in all cases, especially for cirrus clouds. Some pixels used in the study may be contaminated by clouds even after manual screening. The TOA radiances of these pixels are mixtures of surface and cloud top contributions and will be lower than true clear-sky values (Wang *et al*. 2007a, Wan 2008). This is especially true at the Desert Rock site. Air traffic out of Los Angeles produces a considerable amount of cirrus over this site.

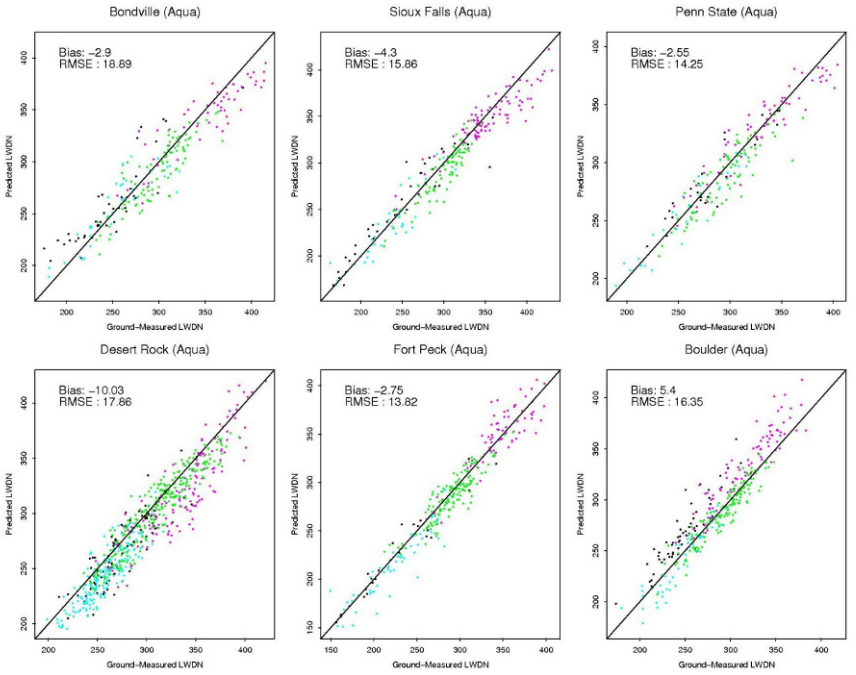

Fig. 6.13 Nonlinear LWDN (downwelling longwave radiation) models validation results using MODIS Aqua data (black: fall-winter/day; cyan: fall-winter/night; magenta: spring-summer/day; green: spring-summer/night).

Although the F_d^l model was developed using MODIS Terra retrieved atmosphere profiles and spectral response functions, it was also applied (without modi-

fication) to two years of MODIS Aqua data (2005 and 2006) because the two sensors have similar designs. Table 6.7 also summarizes the validation results using Aqua data. Figure 6.13 shows the validation plots. The nonlinear models' biases range from -10.03 to 5.40 W/m^2 and RMSEs range from 13.82 to 18.89 W/m^2. Terra and Aqua have different satellite overpass times: 10:30 am and 10:30 pm versus 1:30 pm and 1:30 am (local time). The atmosphere and land surface conditions are different when these two sensors overpass. However, the nonlinear model biases and RMSEs are generally smaller for Aqua. Liu *et al*. (2008) show that the Aqua sensor has smaller systematic errors than Terra in thermal channels, which may contribute to the small errors in Aqua-derived F_d^l. The Aqua validation results indicated that the F_d^l model developed in this study is sufficiently general to be applied for both Terra and Aqua observations.

6.4 Clear-Sky Upward Longwave Radiation

The upward longwave radiation emitted in the spectral wavelengths greater than 4 μm is sometimes referred to as "terrestrial radiation" or "infrared radiation". If we know surface skin temperature (T_S) and spectral emissivities (ε_i) that are converted to broadband emissivity (ε) , we can easily calculate this quantity:

$$F_u^l = F_d^l(1-\varepsilon) + \sigma\varepsilon T_S^4 \tag{6.13}$$

where F_d^l is downward longwave radiation and σ is the Stefan-Boltzmann's constant. We recently published the formulae for converting the MODIS spectral emissivities to broadband emissivity (Wang *et al*. 2005, Jin and Liang 2006).

MODIS has routinely generated skin temperature products globally. The MODIS land team produces the land surface temperature (MOD11) using both a split-window algorithm and day/night algorithm (Wan *et al*. 2002). The MODIS atmospheric team is also producing surface skin temperature at 5 km resolution (MOD07). We have recently validated the MODIS skin temperature products (MOD7 and MOD11) using FLUXNET sites (Wang W. *et al*. 2008) and found that both products agreed reasonably well with ground measurements over vegetated sites, with biases as large as 3.4° K and root-mean square errors (RMSE) 3.8° K in all eight sites investigated. The uncertainties from both skin temperature and broadband emissivity may result in larger errors in the calculated upward longwave radiation.

Our validation results using ground measurements did not prove that this method is better than the hybrid algorithm discussed in Section 6.3 for downward radiation (Wang W. *et al*. 2008). Therefore, we propose to apply the hybrid algorithm in this study.

In fact, Smith and Woolf (1983) used a hybrid method to estimate both F_u^l and F_d^l from the NOAA geostationary satellite's Visible Infrared Spin Scan Radiometer (VISSR) Atmospheric Sounder (VAS) TOA radiance at the 1000 hPa pressure level. Meerkoetter and Grassl (1984) used the hybrid method to estimate F_u^l and surface net longwave radiation from the Advanced Very High Resolution Radiometer (AVHRR) split-window radiance. However, previous studies have focused on estimating surface longwave radiation over sea surfaces and constant emissivity was usually assumed. We used the hybrid method in this study to derive clear-sky F_u^l models for MODIS data over land surfaces. The emissivity effect is explicitly considered in the radiative transfer simulation process.

The simulated databases were analyzed to develop models for predicting F_u^l from TOA radiance. Multiple regression analysis was first employed to develop a linear F_u^l model. It is found that MODIS bands 29, 31, and 32 predict F_u^l best, consistent with the physics that governs F_u^l. All three bands are sensitive to F_u^l variations. Moreover, these three bands differ in water-vapor absorption. Bands 31 and 32 are used to retrieve column water vapor, an important factor in estimating F_u^l from satellite data. The derived linear model is as follows:

$$F_u^l = a_0 + a_1 L_{29} + a_2 L_{31} + a_3 L_{32} \tag{6.14}$$

where a_0, a_1, a_2, and a_3 are regression coefficients (Table 6), and L_{29}, L_{31}, L_{32} are MODIS channels 29, 31, and 32 TOA radiance. Statistical analysis indicates that the linear model accounts for more than 99% of the variation in the simulated databases, with standard errors of 4.89 W/m^2 (0° sensor view zenith angle) to 6.11 W/m^2 (60° sensor view zenith angle).

We evaluated some non-linear models using both TOA radiance and brightness temperature to reduce the nonlinear effect in the residuals, but the models were not significantly improved.

Table 6.6 Summary of linear model fitting results (θ – sensor viewing zenith angle; unit of standard error: w/m^2)

	Linear Regression					
θ	**a_0**	**a_1**	**a_2**	**a_3**	**R^2**	**Std. Err**
0°	102.7589	10.4963	121.3973	-100.4079	0.993	4.89
15°	104.5829	10.6894	123.4974	-103.0277	0.993	4.94
30°	110.4514	11.4267	129.9471	-111.2339	0.992	5.10
45°	122.3125	13.5455	141.1782	-126.4748	0.991	5.41
60 °	146.0408	20.5749	157.2946	-152.6469	0.990	6.11

The validation results were recently published (Wang *et al*. 2009). Figure 6.14 shows the validation results with MODIS Terra data. The linear model has biases ranging from -4.62 to -21.93 W/m^2 and RMSEs ranging from 12.72 to 25.03

W/m^2. The validation method for the Aqua data is the same as that used for Terra data. It has biases ranging from -5.21 to -20.21 W/m^2 and RMSEs ranging from 10.92 to 23.94 W/m^2.

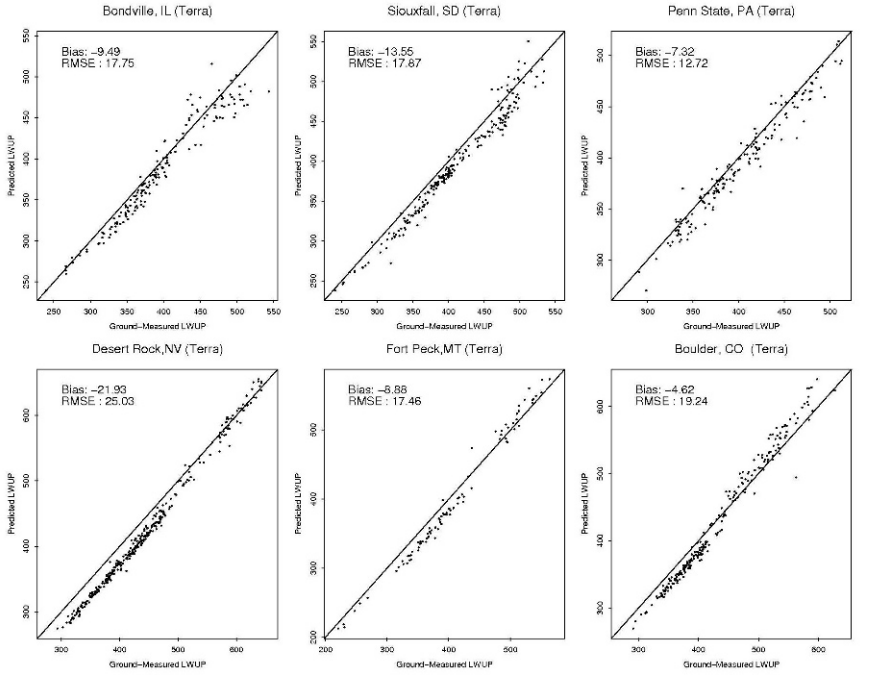

Fig. 6.14 Linear model method validation results using MODIS Terra TOA radiances.

6.5 Clear-Sky Net Longwave Radiation

MODIS-derived surface net longwave radiation validation used the same SURFRAD sites as F_d^l (Wang W. and Liang 2009). Table 6.7 summarizes the validation results. Figure 6.15 illustrates validation results from Terra MODIS data at individual sites. The averaged RMSEs were 17.72 W/m^2 (Terra) and 16.88 W/m^2 (Aqua); the averaged biases are -2.08 W/m^2 (Terra) and 1.99 W/m^2 (Aqua). The RMSEs over all sites are less than 20 W/m^2, the acceptable accuracy for the instantaneous surface longwave radiation budget. Larger scattering exists for daytime observations during spring and summer (high temperature and moisture conditions), similar to the error patterns in F_d^l and surface upward longwave radiation validation results.

Table 6.7 Surface net longwave radaition validation results (unit W/m^2)

Sites	Terra		Aqua	
	Bias	RMSE	Bias	RMSE
Bondville	3.97	19.12	7.67	19.74
Sioux Falls	-2.43	17.08	-1.00	15.60
PennState	1.37	18.92	6.19	18.87
DesertRock	-3.88	18.40	-0.09	16.90
FortPeck	-1.79	13.44	4.70	14.44
Boulder	-9.69	19.38	-5.51	15.75
Mean	-2.08	17.72	1.99	16.88

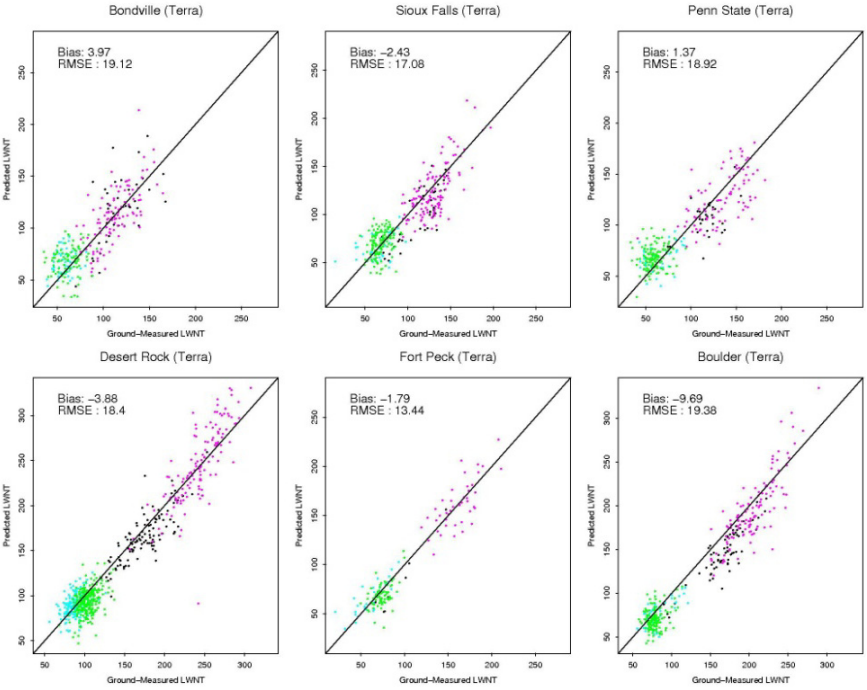

Fig. 6.15 MODIS Terra-derived surface net longwave radiation validation results.

Figure 6.16 compares the MODIS net longwave radiation using the algorithms described above and the corresponding CERES product over the Washington DC and Baltimore Metropolitan region. The MODIS product reveals much more spatial details than the CERES product that has only several values due to its coarse spatial resolution. Note the CERES mean value is also about 23 W/m^2 smaller.

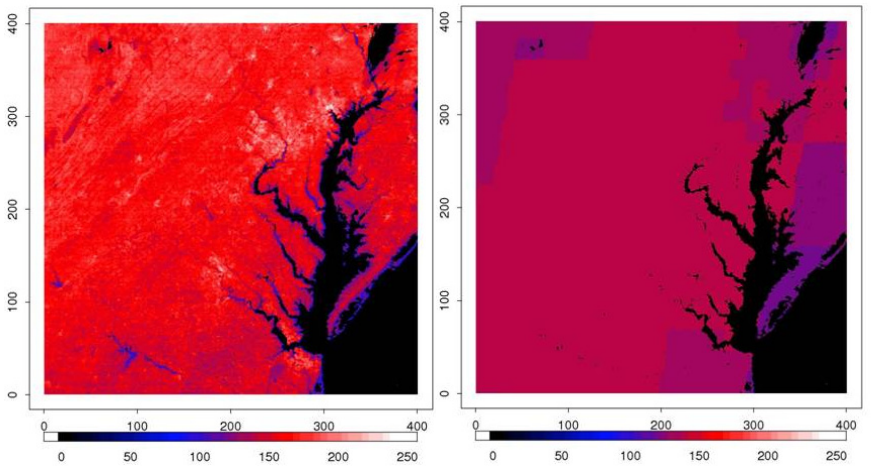

Fig. 6.16 MODIS-derived from Aqua satellite (left) vs. CERES-derived(right) instantaneous clear-sky longwave net radiation (W/m2) images over the Washington D.C. - Baltimore Metropolitan Area (April 10, 2007 18:10 UTC)

6.6 Cloudy-Sky Net Radiation

Sections 6.4 – 6.5 discussed the algorithms for mapping downward and upward longwave radiation under clear-sky conditions. For cloudy-sky conditions, there are many algorithms that have been proposed in the literature (e.g., Diak *et al*. 2004, Zhou and Cess 2001), but we lack confidence that these algorithms are sufficiently mature to generate the products from MODIS during the course of this study. Two empirical formulae have been developed recently.

6.6.1 Instantaneous Value Estimation

An empirical regression method has been developed to estimate instantaneous all-wave net radiation from shortwave net radiation under FLUXNET data under cloudy conditions (Kim, 2008). Cloud-sky measurements at 13 FLUXNET sites were filtered out and their relationship is shown in Figure 6.17. It is highly linear (R_n=0.8347S_n+20.1898), with R^2 = 0.9469 and RMSE =35.1 Wm^{-2}, but the scatters are also significant.

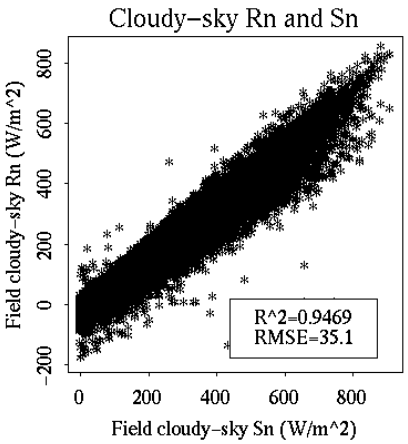

Fig. 6.17 Measured all-wave net radiation and the shortwave net radiation under cloudy-sky conditions

To improve the relationship, we group data in different cover types and add the enhanced vegetation index (EVI) as a new independent variable. The resulting formula is expressed as follows:

$$R_n = a_0 + a_1 EVI + a_2 S_n + a_3 S_n \cdot EVI \tag{6.15}$$

The coefficients for different land cover types are listed in Table 6.8. The estimates are appreciably improved for all cover types except grasslands (see Figure 6.18) because EVI in grass is usually low and the exposed soil and dead grass could increase the outgoing thermal radiation and decrease accuracy.

Table 6.8 Regression coefficients used to estimate cloudy-sky all-wave net radiation

PFT	a_0	a_1	a_2	a_3	R^2	RMSE
Broadleaf crop	*18.57*	*8.05*	*0.76*	*0.19*	*0.9729*	*27.4*
Evergreen needleleaf	*11.84*	*-6.19*	*0.86*	*0.03*	*0.9736*	*28.9*
Grass	*-35.46*	*36.39*	*0.66*	*0.46*	*0.9339*	*43.1*
Deciduous broadleaf	*-14.40*	*-15.32*	*0.74*	*0.24*	*0.9605*	*31.9*

6.6.2 Daily Value Estimation

Kjaersgaard *et al*. (2007) compared six existing models for calculating daytime Rn from solar shortwave radiation using meteorological data at two temperate sites, and concluded that local calibration of the models with at least five years of data is essential to obtain stable calibration coefficients. However, all six methods

failed to consider surface characteristics (such as vegetation cover fraction) that have substantial effects on surface energy partitioning into latent and sensible heat fluxes (Wang *et al*. 2007c, Wang and Liang 2008a) which in turn, affect T_s and F_u^l (Wang *et al*. 2006, Wang *et al*. 2007b).

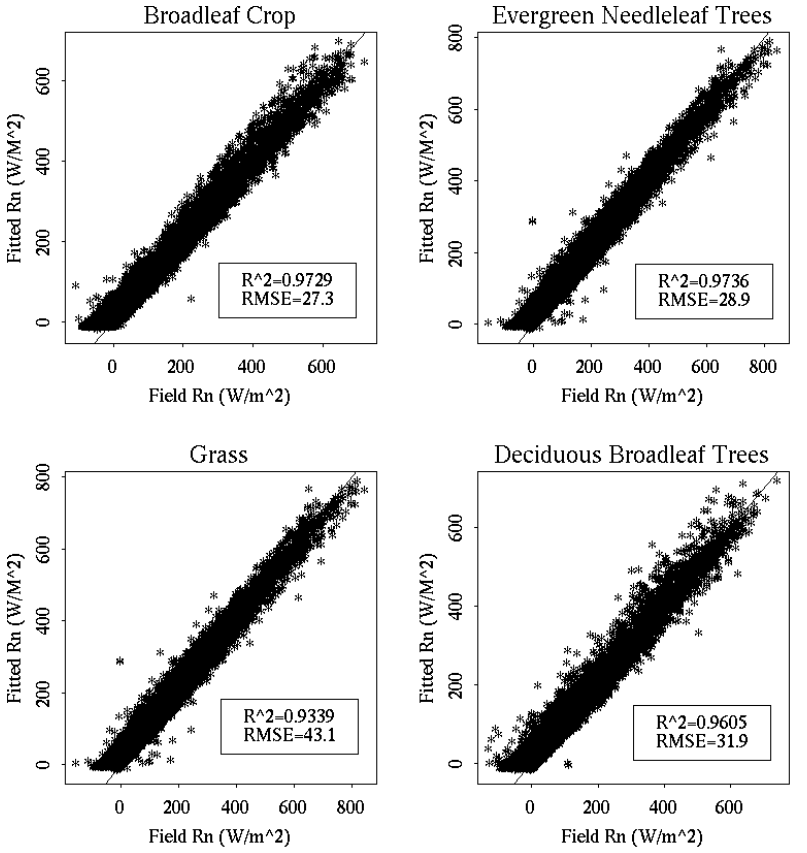

Fig. 6.18 Cloudy-sky all-wave net radiation fitting dependant on plant functional types

Therefore, based on analysis of available long-term measurements, we proposed a robust method to estimate R_n from all-sky shortwave radiation (Wang K. and Liang 2009a). The equation is as follows:

$$\left(\frac{R_n}{S_n}\right) = a_0 + a_1 \cdot T_{\min} + a_2 \cdot DTR + a_3 \cdot VI + a_4 \cdot RH \tag{6.16}$$

where T_{min} is daily minimum T_a (or T_s), DTR is daily T_a (or T_s) range, VI is the MODIS global $NDVI$ (Normalized Difference Vegetation Index) or EVI product

with a spatial resolution of 1 km and a 16-day temporal resolution, and RH (Relative Humidity) is relative humidity. To incorporate the elevation contribution, the T_{min} used in equation (6.16) is corrected to sea level by decreasing temperature 6.5 ºC for each 1-km increase in elevation.

Since the relationships between R_n/S_n and DTaR (Diurnal air Temperature Range), Tamin, VI, and RH are not exactly linear, none of these parameters can individually account for the variance in R_n/S_n although the four parameters in combination estimate the variance in R_n/S_n with greater accuracy. We also performed the regression analysis with the square of the terms in addition to the linear terms but could not improve the results substantially.

In the equation, near surface air temperature and DTaR are input parameters. These parameters are difficult to obtain at satellite pixel scale with reasonable accuracy. Fortunately, the algorithm is not very sensitive to these parameters and they can be obtained from GMAO (Globally Modeling and Assimilation Office , http://gmao.gsfc.nasa.gov/).

The strength of this method is that it accurately estimates R_n for a wide variety of land cover types and climates, and a range of surface elevations, without local calibration.

The validation results are described in a recent paper (Wang K. and Liang, 2009a). The data collected at twenty-four sites of three networks (ARM, SURFRAD and FLUXNET) have been used for validation. We used the Amdo, Bondville, Desert Rock, EF02, EF07, EF12, EF15, EF18, EF19, Fort Peck, Penn State, and Sioux Falls data to derive the coefficients in equation (6.16), and validated the coefficients with the Boulder, Gaize, EF04, EF08, EF09, EF13, EF20, EF22, EF26, EF27, Goodwin Creek and Wind River data. Table 6.9 lists the derived coefficients.

Table 6.9 The fitted parameters in equation (6.16) and the statistics for all 24 sites. Equation (6.16) is used to predict daytime Rn at all 24 sites using the parameters shown in the following columns. The correlation coefficients and RMSE between measured and predicted daytime Rn are given in the last two lines. DTsR: Diurnal land surface Temperature Range; DTaR: Diurnal air Temperature Range

Combinations of parameters	NDVI, Ts min, DTsR, RH	NDVI, Ta min, DTaR, RH	EVI, Ts min, DTsR, RH	EVI, Ta min, DTaR, RH
a0	0.5749	0.5129	0.5842	0.5195
a1	0.0026	0.0025	0.0026	0.0024
a2	-0.0018	0.0000	-0.0018	0.0001
a3	0.1299	0.1401	0.1813	0.1944
a4	0.2053	0.2604	0.2063	0.2651
Correlation coefficient	0.99	0.99	0.99	0.99
RMSE	16.9(6%)	17.6 (7%)	17.0 (6%)	17.8 (7%)

Equation (6.16) and Table 6.9 coefficients accurately estimate R_n for a range of land cover types, surface elevations, and climates without local calibration. The bias varies from -7.8 W m^{-2} to +9.7 W m^{-2} (± 3% in relative value) for different sites. The RMSE varies from 12.8 W m^{-2} to 21 W m^{-2} (from 5% to 9% in relative value) for different sites and an average of 16.9 W m^{-2} (6% in relative value) for all the sites, and the correlation coefficient is about 0.99 for all the sites.

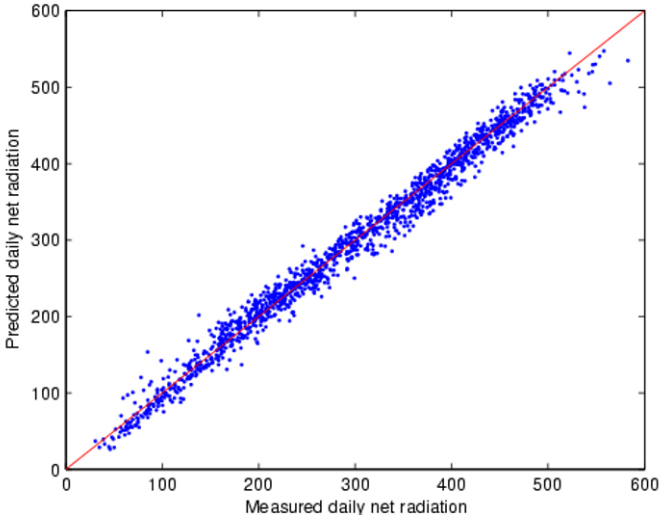

Fig. 6.19 Scatterplot of measured and predicted daytime R_n calculated with Equation (6.16) using daily minimum land surface temperature (Ta min), daily land surface temperature range (DTR), relative humidity (RH), and NDVI using data collected at Pawhuska, Oklahoma (EF12) from 2002 to 2006.

Both EVI and NDVI can be used to estimate R_n. Our previous studies also show that T_s is directly related to $F_u^{\ l}$ while the relationship between T_a and $F_u^{\ l}$ is indirect (Wang *et al*., 2005, 2007c, 2008a). Since satellite T_s retrieval is not available under cloudy conditions, we provide an equation using T_a under cloudy conditions.

6.7 All-Wave All-Sky Net Radiation

When we calculate all-wave all-sky net radiation, the errors associated with each individual component may not be a simple addition. To assess the uncertainty of the final product, SURFRAD ground measurements were also used. Figure 6.20 illustrates the preliminary validation results from six SURFRAD sites. It seems the calculated product matches the ground measurements very well. There is a slightly nonlinear pattern, but more extensive validation is still going on.

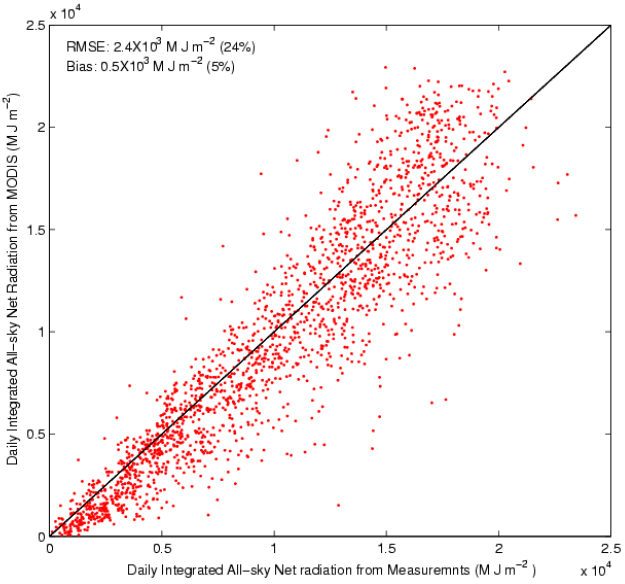

Fig. 6.20 Validation of all-sky all-wave net radiation at six SURFRAD sites in 2005

6.8 Summary

High-resolution land surface radiative fluxes are greatly desired by many land surface models and applications. We have developed a series of algorithms for estimating 1-km daily radiative fluxes from MODIS data, which include incident all-sky PAR insolation and shortwave net radiation, clear-sky upward and downward longwave radiation, cloudy-sky longwave net radiation, and all-wave all-sky net radiation. All of the algorithms have been published. Extensive validation activities have been carried out and the results indicate that these algorithms can be used for generating global high-resolution radiation fluxes accurately. Some of the algorithms have already been used to produce these radiation fluxes on the regional scale. More extensive validation activities will continue.

Those users wishing to characterize land surface biogeophysical and biogeochemical processes at fine spatial resolution should consider using these data sets because they are the only data sets available at such a spatial resolution.

Acknowledgements

This study is supported by NASA under grant NNX08AC53G. Several students have also contributed to data processing and product validation, including Mark Plavnieks, Erica Hafer, and Jennifer Himmelstein.

References

Annear, R. L., and S. A. Wells (2007), A comparison of five models for estimating clear-sky solar radiation, *Water Resource Research*, 43, W10415, doi:10.1029/2006WR005055.

ASDC.(2006), http://eosweb.larc.nasa.gov/HPDOCS/projects/rad_budg.html [visited Dec.22, 2006].

ASTER. (1999), http://speclib.jpl.nasa.gov/ [visited Nov. 30, 2005].

Berg, A.A., J.S. Famiglietti, M. Rodell, R.H. Reichle, U. Jambor, S.L. Holl and P.R. Houser (2005), Development of a hydrometeorological forcing data set for global soil moisture estimation, *International Journal of Climatology*, 25(13): 1697-1714.

Berk, A., Bernstein, L. S., Anderson, G. P., Acharya, P. K., Robertson, D. C., Chetwynd, J. H., & Adler-Golden, S. M. (1998), MODTRAN cloud and multiple scattering upgrades with application to AVIRIS, *Remote Sensing of Environment*, 65, 367– 375.

Betts, A.K., Ball, J.H., Beljaars, A.C.M., Miller, M.J. and Viterbo, P.A., (1996). The land surface-atmosphere interaction: A review based on observational and global modeling perspectives. *Journal of Geophysical Research*, 101(D3): 7209-7225.

Bisht, G., V. Venturini, S. Islama, L. Jiang (2005), Estimation of the net radiation using MODIS (Moderate Resolution Imaging Spectroradiometer) data for clear sky days, *Remote Sensing of Environment*, 97, 52 – 67.

Carder, K., Hawes, S. and Chen, R. (1999), Instantaneous photosynthetically available radiation and absorbed radiation by phytoplankton, Version 5. ATBD-MOD-20.

Chandrasekhar, S. (1960), Radiative Transfer, Dover, Mineola, N. Y.

Charlock, T., (2006), CAVE: Clouds & Radiative Swath (CRS) Footprint Validation, NOAA. Available: http://www-cave.larc.nasa.gov/cave/.

Charlson, R. J., F. P. J.Valero, J. H. Seinfeld (2005), In search of balance. *Science*, 308, 806-807.

Cleugh, H. A., Leuning, R., Mu, Q., & Running, S. W. (2007), Regional evaporation estimates from flux tower and MODIS satellite data. *Remote Sensing of Environment*, 106, 285−304.

Coll, C., E. Valor, R. Niclòs, J. M. Sánchez, R. Rivas, V. Caselles, and J. M. Galve (2005), Ground measurements for the validation of land surface temperatures derived from AATSR and MODIS data, *Remote Sensing of Environment*, 97, 288-300.

Dai, Y. *et al*., (2003), The Common Land Model (CLM), *Bulletin of American Meteorological Society*, 84(8), 1013.

Darnell, W.L., Gupta, S.K. and Staylor, W.F. (1986), Downward longwave surface radiation from sun-synchronous satellite data: Validation of methodology. *Journal Climate and Applied Meteorology*, 25, 1012-1021.

Diak, G.R. *et al*. (2004), Estimating land surface energy budgets from space - Review and current efforts at the University of Wisconsin-Madison and USDA-ARS. *Bulletin of the American Meteorological Society*, 85(1), 65-75.

Dickinson, R.E. (1995). Land atmosphere interaction. *Reviews of Geophysics*, Suppl.: 917-922.

Duchon, C. E., and O. Malley (1999), Estimating Cloud Type from Pyranometer Observations. *Journal of Applied Meteorology*, 38, 132-141.

Dye, D. (2004), Spectral composition and quanta-to-energy ratio of diffuse photosynthetically active radiation under diverse cloud conditions. *Journal of Geophysical Research*, 109, D10203, doi:10.1029/2003JD004251.

Eck, T. F., and D. G. Dye (1991), Satellite estimation of incident photosynthetically active radiation using ultraviolet reflectance, *Remote Sensing of Environment*, 38, 135– 146.

Ellingson, R.G. (1995), Surface longwave fluxes from satellite observations: A critical review, *Remote Sensing of Environment*, 51, 89-97.

Forsythe, W. C., Rykiel, E. J., Stahl, R. S., Wu, H.-i. and Schoolfield, R. M. (1995), A model comparison for daylength as a function of latitude and day of year. *Ecological Modelling*, 80, 87-95.

Francis, J., and J. Secora. (2004), A 22-year dataset of surface longwave fluxes in the Arctic. *Fourteenth ARM Science Team Meeting Proceedings*, March 22-26, at Albuquerque, NM.

Frouin, R. & Pinker, R. T. (1995), Estimating photosynthetically active radiation (PAR) at the earth's surface from satellite observations. *Remote Sensing of Environment*, 51, 98-107.

Frouin, R., Lingner, D. W., Gautier, C., Baker, K. S., & Smith, R. C. (1989). A simple analytical formula to compute clear sky total and photosynthetically available solar irradiance at the ocean surface. *Journal of Geophysical Research*, 94(C7), 9731– 9742.

Frouin, R., Franz, B. and Wang, M., (2000). Algorithm to estimate PAR from SeaWiFS data, Version 1.0 - Documentation.

Garratt, J.R., Krummel, P. and Kowalczyk, E.A. (1993), The surface energy balance at local and regional scales - A comparison of general circulation model results with observations. *Journal of Climate*, 6, 1090-1109.

Gu, L. *et al*., (2002). Advantages of diffuse radiation for terrestrial ecosystem productivity. *Journal of Geophysical Research*, 107(D6), 4050, doi:10.1029/2001JD001242.

Gu, L.H. *et al*. (2003), Response of a deciduous forest to the Mount Pinatubo eruption: Enhanced photosynthesis. *Science*, 299: 2035-2038.

Gu, J., Smith, E. A., Cooper, H. J., Grose, A., Liu, G., Merritt, J. D., Waterloo, M. J., de Araújo, A. C., Nobre, A. D., Manzi, A. O., Marengo, J., de Oliveira, P. J., von Randow, C., Norman, J., & Silva Dias, P. (2004), Modeling Carbon Sequestration over the Large-Scale Amazon Basin, Aided by Satellite Observations. Part I: Wet- and Dry-Season Surface Radiation Budget Flux and Precipitation Variability Based on GOES Retrievals. *Journal of Applied Meteorology*, 43(6), 870–886.

Gupta, S.K., Darnell, W.L. and Wilber, A.C. (1992), A parameterization for longwave surface radiation from satellite data: Recent improvements. *Journal of Applied Meteorology*, 31, 1361-1367.

Hicke, J.A. (2005), NCEP and GISS solar radiation data sets available for ecosystem modeling: Description, differences, and impacts on net primary production, *Global Biogeochemical Cycles*, 19, GB2006, doi:10.1029/2004GB002391.

Inamdar, A.K., and V. Ramanathan, Clouds and the Earth's Radiant Energy System (CERES) algorithm theoretical basis document: estimation of longwave surface radiation budget from CERES (subsystem 4.6.2), 1997.

Jin, M., S. Liang (2006), Improved emissivity parametrization for land surface modeling using global remote sensing observations, *Journal of Climate*, 19(12), 2867-2881.

Kaufman, Y. J., D. Tanre´, L. Remer, E. F. Vermote, A. Chu, and B. N. Holben (1997a), Operational remote sensing of tropospheric aerosol over the land from EOS-MODIS., *Journal of Geophysical Research*, 102(D14), 17,051 –17,068.

Kaufman, Y. J., A. Wald, L. A. Lorraine, B. C. Gao, R. R. Li, and L. Flynn (1997b), Remote sensing of aerosol over the continents with the aid of a 2.2 um channel, *IEEE Transactions on Geoscience and Remote Sensing*, 35, 1286– 1298.

Kim, H. Y., (2008), Estimation of Land Surface Shortwave Radiation Budget from MODIS Data, Ph.D dissertation, Department of Geography, University of Maryland

Kjaersgaard, J. H., R. H. Cuenca, F. L. Plauborg, S. Hansen (2007), Long-term comparisons of net radiation calculation schemes. Boundary-Layer Meteorology, 123, 417–431.

Lee, H.T. and Ellingson, R.G. (2000), Development of a nonlinear statistical method for estimating the downward longwave radiation at the surface from satellite observations, *Journal of Atmospheric and Oceanic Technology*, 19(10), 1500- 1515.

Liang, S. (2004), Quantitative Remote Sensing of Land Surfaces, 534 pp., John Wiley, Hoboken, N. J.

Liang, S., T. Zheng, R. Liu, H. Fang, S. C. Tsay, S. Running, (2006), Estimation of incident Photosynthetically Active Radiation from MODIS Data, *Journal of Geophysical Research*, 111, D15208,doi:10.1029/2005JD006730.

Liang, S. T. Zheng, D. Wang, K. Wang, R. Liu, S. C. Tsay, S. Running, J. Townshend, (2007), Mapping High-Resolution Incident Photosynthetically Active Radiation over Land from Polar-Orbiting and Geostationary Satellite Data, *Photogrammetric Engineering and Remote Sensing*, 73(10), 1085-1089.

Liepert, B.G. and Romanou, A. (2005), Global dimming and brightening and the water cycle. *Bulletin of the American Meteorological Society*, 86(5), 622-623.

Liu, R., S. Liang, H. He, J. Liu, and T. Zheng (2008), Mapping Photosynthetically Active Radiation from MODIS Data in China. *Remote Sensing of Environment*, 112, 998-1009.

Meerkoetter, H. and H. Grassl (1984),Longwave net flux at the ground from radiance at the top, presented at *IRS '84 current problems in atmospheric radiation; proceedings of the International Radiation Symposium*, Perugia, Italy, 1984.

Morcrette, J. J., and P. Y. Deschamps. (1986). Downward longwave radiation at the surface in clear sky atmospheres: comparison of measured, satellite-derived and calculated fluxes. *Proc. ISLSCP Conf*, at Rome, ESA SO-248M Darmstadt, Germany.

Mu, Q., F. A. Heinsch, M. Zhao, S. W. Running (2007), Development of a global evapotranspiration algorithm based on MODIS and global meteorology data. *Remote Sensing of Environment*, 111, 519-536.

Pinker, R.T. and Laszlo, I. (1992), Modeling surface solar irradiance for satellite applications on a global scale, *Journal of Applied Meteorology*, 31: 194-211.

Pinker, R. T., *et al*. (2003), Surface radiation budgets in support of the GEWEX Continental-Scale International Project (GCIP) and the GEWEX Americas Prediction Project (GAPP), including the North American Land Data Assimilation System (NLDAS) project, *Journal of Geophysical Research*, 108(D22), 8844, doi:10.1029/2002JD003301.

Prince, S.D. and S.N. Goward (1995), Global primary production: a remote sensing approach, *Journal of Biogeography*, 22(4-5), 815-835.

Raschke, E., Bakan, S. and Kinne, S., 2006. An assessment of radiation budget data provided by the ISCCP and GEWEX-SRB. *Geophysical Research Letters*, 33, L07812, doi:10.1029/2005GL025503.

Remer, L.A. *et al*. (2005) The MODIS aerosol algorithm, products, and validation. *Journal of the Atmospheric Sciences*, 62(4), 947-973.

Remer, L. A., *et al*. (2008), Global aerosol climatology from the MODIS satellite sensors, *Journal of Geophysical Research*, 113, D14S07, doi:10.1029/2007JD009661.

Running, S.W., Nemani, R., Glassy, J.M. and Thornton, P. (1999), MODIS PSN (net photosynthesis) and NPP (net primary productivity) products, Version 3.0. MOD17 PSN/NPP Algorithm Technical Basis Document.

Running, S., Nemani, R.R., Heinsch, F.A., Zhao, M., Reeves, M., & Hashimoto,H. (2004), A continuous satellite-derived measure of Global terrestrial primary production. *Bioscience*, 54, 547−560.

Salomonson, V., W. Barnes, P. Maymon, H. Montgomery, and H. Ostrow (1989), MODIS: advanced facility instrument for studies of the Earth as a system. *IEEE Transactions on Geoscience and Remote Sensing*, 27, 145–153.

Schaaf, C., Gao, F., Strahler, A., Lucht, W., Li, X., Tsung, T., Strugll, N., Zhang, X., Jin, Y., Muller, P., Lewis, P., Barnsley, M., Hobson, P., Disney, M., Roberts, G., Dunderdale, M., Doll, C., d'Entremont, R., Hu, B., Liang, S., Privette, J., & Roy, D. (2002). First operational BRDF, albedo nadir reflectance products from MODIS. *Remote Sensing of Environment, 83*, 135-148.

Schmetz, J., (1989), Towards a surface radiation climatology: retrieval of downward irradiances from satellites, *Atmospheric Research*, 23, 287-321.

Seemann, Suzanne W., Jun Li, W. Paul Menzel, and Liam E. Gumley (2003), Operational retrieval of atmospheric temperature, moisture, and ozone from MODIS infrared radiances, *Journal of Applied Meteorology*, 42(8), 1072-1091.

Sellers, P.J. *et al*. (1996), A revised land surface parameterization (SiB2) for Atmospheric GCMs. Part II: The generation of global fields of terrestrial biophysical parameters from satellite data. *Journal of Climate*, 9, 706-737.

Smith, W. L., and H. M. Wolfe (1983), Geostationary satellite sounder (VAS) observations of longwave radiation flux. *The Satellite Systems to Measure Radiation Budget Parameters and Climate Change Signal*, 29 Aug - 2 Sep, at Igls, Austria.

Van Laake, P. E., & Sanchez-Azofeifa, G. A. (2004). Simplified atmospheric radiative transfer modelling for estimating incident PAR using MODIS atmosphere products. *Remote Sensing Environment*, 91, 98–113.

Van Laake, P. E., & Sanchez-Azofeifa, G. A. (2005). Mapping PAR using MODIS atmosphere products. *Remote Sensing of Environment*, 94(4), 554– 563.

Viterbo, P. and Beljaars, C. (1995), An improved land surface parametrization scheme in the ECMWF model and its validation, *Journal of Climate*, 8, 2716-2748.

Vermote, E. F., Tanré, N. Z., Deuzé, J. L., Herman, M., & Morcette, J. J. (1997), Second simulation of the satellite signal in the solar spectrum: An overview. *IEEE Transactions on Geoscience and Remote Sensing*, 35, 675-686.

Wan, Z. and J. Dozier. (1996), A generalized split-window algorithm for retrieving land-surface temperature from space. *IEEE Transactions on Geoscience and Remote Sensing*, 34(4), 892-905.

Wan, Z. (1999), MODIS land-surface temperature algorithm theoretical basis document (LST ATBD): version 3.3, University of California, Santa Barbara, Santa Barbara, CA, 1999.

Wan, Z., Y.-L. Zhang, Q.-C. Zhang, and Z.-L. Li (2002), Validation of the land surface temperature products retrieved from terra moderate resolution imaging spectroradiometer data, *Remote Sensing of Environment*, 83, 163–180.

Wan, Z., Y. Zhang, Q. Zhang, and Z. L. Li, (2004), Quality assessment and validation of the MODIS global land surface temperature *International Journal Remote Sensing*, 25, 261-274.

Wan, Z. (2008), New refinements and validation of the MODIS land-surface temperature/emissivity products, *Remote Sensing of Environment*, 112, 59-74.

Wang, D., S. Liang and T. Zheng, (2009), Estimation of daily-integrated PAR from sparse satellite observations: comparison of temporal scaling methods, *International Journal of Remote Sensing*, in press.

Wang, K., Z. Wan, P. Wang, M. Sparrow, J. Liu, X. Zhou, and S. Haginoya (2005), Estimation of surface long wave radiation and broadband emissivity using Moderate Resolution Imaging Spectroradiometer (MODIS) land surface temperature/emissivity products, *Journal of Geophysical Research*, 110, D11109, doi:10.1029/2004JD005566.

Wang, K., Z. Li, and M. Cribb (2006), Estimation of evaporative fraction from a combination of day and night land surface temperature and NDVI: A new method to determine the Priestley–Taylor parameter, *Remote Sensing of Environment*, 102, 293-305.

Wang, K., Z. Wan, P. Wang, M. Sparrow, J. Liu, and S. Haginoya (2007a), Evaluation and improvement of the MODIS land surface temperature/emissivity products using ground-based measurements at a semi-desert site on the western Tibetan Plateau. *International Journal Remote Sensing*, 28, 2549 - 2565.

Wang, K., J. Wang, P. Wang, M. Sparrow, J. Yang, and H. Chen, (2007b), Influences of urbanization on surface characteristics as derived from the Moderate-Resolution Imaging Spectroradiometer: A case study for the Beijing metropolitan area. *Journal of Geophysical Research*, 112, D22S06, doi:10.1029/2006JD007997.

Wang, K., P. Wang, Z. Li, M. Cribb, and M. Sparrow (2007c) A simple method to estimate actual evapotranspiration from a combination of net radiation, vegetation index, and temperature, *Journal of Geophysical Research*, 112, D15107, doi:10.1029/2006JD008351.

Wang, K., and S. Liang (2008), An improved method for estimating global evapotranspiration based on satellite determination of surface net radiation, vegetation index, temperature, and soil moisture, *Journal of Hydrometeorology*, 9, 712-727.

Wang, K., R. E. Dickinson, and S. Liang (2008), Observational evidence on the effects of clouds and aerosols on net ecosystem exchange and evapotranspiration, *Geophysical Research Letter*, 35, L10401, doi:10.1029/2008GL034167.

Wang, K., R. E. Dickinson, S. Liang, (2009), Clear Sky Visibility Has Decreased over Land Globally from 1973 to 2007, *Science*, 323, 1468-1470.

Wang, K., S. Liang (2009a), Estimation of daytime net radiation from shortwave radiation measurements and meteorological observations, *Journal of Applied Meteorology and Climatology*, 48:634-643.

Wang, K. and S. Liang, (2009b), Evaluation of ASTER and MODIS land surface temperature and emissivity products using surface longwave radiation observations at SURFRAD sites, *Remote Sensing of Environment*, 113:1156-1165.

Wang, K., S. Liang, T. Zheng and D. Wang (2009). Simultaneous estimation of surface photosynthetically active radiation and albedo from GOES, *Remote Sensing of Environment*, revised.

Wang, W., S. Liang, and T. Meyer, (2008), Validating MODIS land surface temperature products, *Remote Sensing of Environment*, 112, 623-635

Wang, W., S. Liang, J. A. Augustine, (2009), Estimating clear-sky land surface upward longwave radiation from MODIS data, *IEEE Transactions on Geoscience and Remote Sensing*, 47(5):1555-1570, DOI: 10.1109/TGRS.2008.2005206.

Wang, W. & S. Liang, (2009), Estimating High-Spatial Resolution Clear-Sky Land Surface Downwelling Longwave Radiation from MODIS Data, *Remote Sensing of Environment*, 113:745-754.

Wielicki, B.A. *et al*. (1998), Clouds and the Earth's Radiant Energy System (CERES): Algorithm overview. *IEEE Transactions on Geosciences and Remote Sensing*, 36, 1127-1141.

Wild, M. *et al*. (2005), From dimming to brightening: Decadal changes in solar radiation at Earth's surface. *Science*, 308, 847-850.

Wild, M., A. Ohmura, and K. Makowski, (2007), Impact of global dimming and brightening on global warming, *Geophysical Research Letters*, 34, L04702, doi:10.1029/2006GL028031

Winslow, J.C., Hunt, E.R.J. and Piper, S.C. (2001), A globally applicable model of daily solar irradiance estimated from air temperature and precipitation data. *Ecological Modelling*, 143, 227-243.

Yang, K., Koike, T., Stackhouse, P., Mikovitz, C., & Cox, S. J. (2006). An assessment of satellite surface radiation products for highlands with Tibet Instrumental data. *Geophysical Research Letter*, 33, L22403, doi: 10.1029/2006GL027640.

Yang, K., R. T. Pinker, Y. Ma, T. Koike, M. M. Wonsick, S. J. Cox, Y. Zhang, and P. Stackhouse (2008), Evaluation of satellite estimates of downward shortwave radiation over the Tibetan Plateau, *Journal of Geophysical Research*, 113, D17204, doi:10.1029/2007JD009736.

Zhang, Y.C., Rossow, W.B., Lacis, A.A., Oinas, V. and Mishchenko, M.I., (2004), Calculation of radiative fluxes from the surface to top of atmosphere based on ISCCP and other global data sets: Refinements of the radiative transfer model and the input data. *Journal of Geophysical Research*, 109, D19105, doi:10.1029/2003JD004457.

Zhang, Y., W. B. Rossow, and P. W. Stackhouse Jr., (2007), Comparison of different global information sources used in surface radiative flux calculation: Radiative properties of the surface. *Journal of Geophysical Research*, 112, D01102, doi:10.1029/2005JD007008.

Zhao, M., S. Running and R. Nemani, (2006), Sensitivity of Moderate Resolution Imaging Spectroradiometer (MODIS) terrestrial primary production to the accuracy of meteorological reanalyses, *Journal of Geophysical Research*, 111: G01002, doi:10.1029/2004JG000004.

Zheng, T., Liang, S. and Wang, K., (2008), Estimation of incident PAR from GOES imagery. *Journal of Applied Meteorology and Climatology*, 47, 853-868.

Zhong, B., S. Liang, and B. Holben, (2007), Validating a New Algorithm for Estimating Aerosol Optical Depths over Land from MODIS Imagery, *International Journal of Remote Sensing*, 28(18), 4207-4214.

Zhou, Y.P. and Cess, R.D. (2001), Algorithm development strategies for retrieving the downwelling longwave flux at the Earth's surface. *Journal of Geophysical Research*, 106(D12): 12477-12488.